RSC Advances

ROYAL SOCIETY OF CHEMISTRY

www.rsc.org/advances

A novel method to prepare three-dimensional graphene-wrapped PANI nanofiber composite with high supercapacitive performance is supplied in this work.

RSC Advances

RSC Publishing

ARTICLE

Three-dimensional graphene-wrapped PANI nanofiber composite as electrode material for supercapacitor

Cite this: DOI: 10.1039/x0xx00000x

Received 07th November 2014,
Accepted 00th January 2014

DOI: 10.1039/x0xx00000x

www.rsc.org/advances

Jiande Wang[a,b,†], Haiyang Xian[a,†], Tongjiang Peng[a,*], Hongjuan Sun[a],

Fengxian Zheng[c]

A novel three-dimensional graphene/polyaniline (3DGP) composite was achieved by hydrothermal method from in-situ polymerization polyaniline/graphene oxide composite and GO suspension. This 3DGP composite possesses a 3D porous network structure and large specific capacity of 648 F g^{-1} at a current density of 0.5 A g^{-1}. Particularly, the capability can reach 356 F g^{-1} even at 20.0 A g^{-1}, 537 F g^{-1} at 1.0 A g^{-1} can also be achieved after 1000 cycles. Therefore, the 3DGP composite is quite a suitable and promising electrode material for supercapacitors.

Introduction

Supercapacitors, which are always called electrochemical capacitors, are considered as a new type of future power storage devices because of their outstanding cycle stability and high power density[1, 2]. They can be basically classified into three kinds, the electric double-layer capacitor (EDLC)[3-5], pseudocapacitor[5-7] and hybrid systems incorporating combinations of double layer and pseudocapacitance[8, 9]. EDLCs store energy through ion adsorption, in other words, the charge accumulations are achieved with electrostatically positive and negative charges separately residing on interfaces between electrolyte and electrodes[10], but the energy densities of EDLCs are too low for many important applications[11]. Pseudocapacitors utilize fast and reversible redox reactions at the surface or in the bulk phase of electrode materials to obtain high capacitance[12]. Carbon materials are currently the most widely utilized active materials in commercial EDLCs[13, 14]. Transition metal oxides (notably ruthenium oxide)[15-17], and the family of conducting polymers, such as polyaniline (PANI), polypyrrole (PPy) are the most commonly investigated classes of pseudocapacitive materials[8, 18-24].

Combining with the advantages of both EDLC and pseudocapacitor, abundant of graphene/PANI composites were reported for supercapacitors[25-30]. Shi et al. [31] reported a kind of graphene/PANI film which has the capacity of 210 F g^{-1} at 0.3 A g^{-1}. Liu et al.[32] and Zhou et al.[33] use the electrostatic adsorption method to prepare graphene/PANI electrode material, the capacity of the obtained materials can reach 301 F g^{-1}. Li et al.[34] use in-situ polymerization to prepare graphene/PANI composite, which proved that the improvement of the supercapacitive performance due to the high conductivity and surface area of graphene. Wang et al.[35], Feng et al.[36] and Hu et al.[37] use the electrochemical deposition method to prepare graphene/PANI composite and it also has good supercapacitive performance.

Recently, 3D porous graphene framework were reported with high surface area[38, 39]. High surface is deemed to be good for enhancing the supercapacitive performance. Xu et al.[40] developed a convenient one-step strategy to prepare functionalized grapheme hydrogels incorporating hydroquinones into the high-surface-area 3D graphene framework, and the functionalized 3D graphene materials exhibit well for electrochemical energy storage and flexible electronics. Niu et al.[41] prepared 3D porous graphene hybrid architectures decorated with various nanomaterials which include PANI.

However, much attention has been paid on the preparation method of graphene/PANI or 3D graphene framework, few researches investigated how to disperse PANI in the 3D graphene framework evenly. Therefore, designing a 3D graphene structure and PANI disperses evenly which is conducive to charge transfer and diffusion of electrolyte can improve the supercapacitive performance of graphene/PANI effectively. In this work, a novel three-dimensional graphene/PANI (3DGP) composite, in which the PANI is coated with grapheme was achieved by hydrothermal method from in-situ polymerization PANI/GO composite and GO suspension, the morphology, structure and supercapacitive performance of the composite were investigated. The example radar plots shown in Fig.1 compare the major metrics of performance of PANI, rGO and 3DGP. In general, a larger area encompassed within a radar plot indicates better overall performance. As is shown in Fig.1, 3DGP exhibits a larger area, indicating better performance than pure PANI and rGO.

Experimental

1. Preparation of graphite oxide

Graphite oxide was prepared by a modified Hummers method based on previously described procedures[42]. Firstly, flake graphite powder (1 g, -200 mesh) was added to concentrated

H_2SO_4 (95%-98%, 23 mL), and the mixture was cooled down to 0 ˚C by using an ice bath, then $KMnO_4$ (4 g) was added slowly to keep the reaction temperature below 15 ˚C for 0.5 h. Secondly, the reaction mixture was heated to 35 ˚C and stirred for 2 h, at which ultrapure water was added slowly, giving rise to a pronounced exothermal effect up to 70˚C±. The reaction mixture was stirred for 30 min, and then 5% of H_2O_2 was added until no gas produced and, finally, the mixture was deposited for 12h, until the supernatant being decanted away. The remaining material was then washed with ultrapure water and deposited again, this process being repeated until the pH was neutral. The graphite oxide gel was obtained after the redundant water was decanted away.

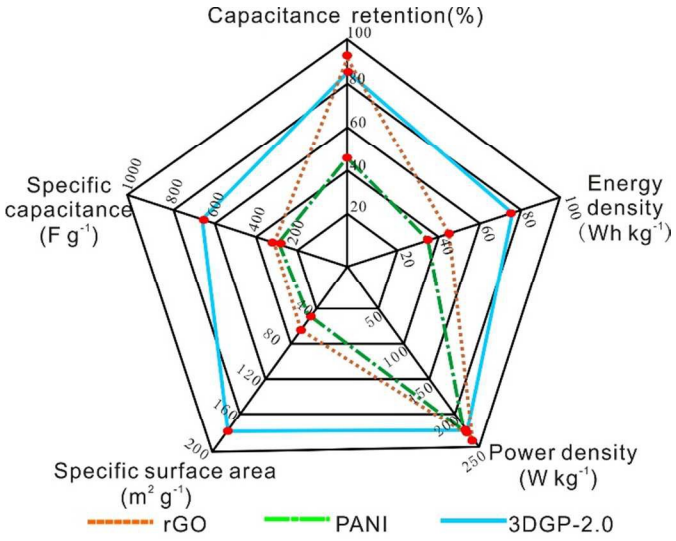

Fig. 1 Radar plots to compare the major metrics of performance of PANI, rGO and 3DGP.

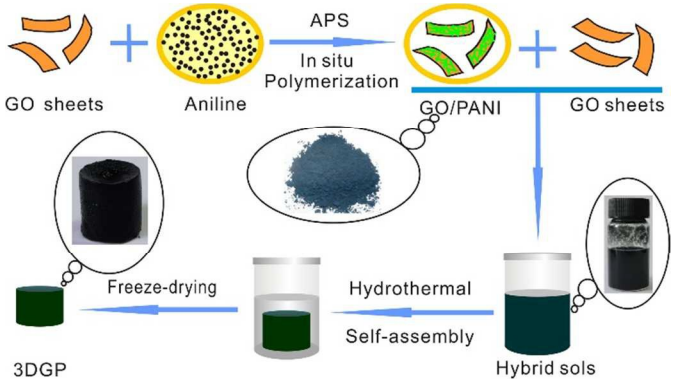

Fig. 2 Illustrations of the preparation processes of PANI and 3DGP.

2. Preparation of three-dimensional graphene-wrapped PANI nanofiber composite (3DGP)

The preparation method is illustrated in Fig. 2. Firstly, graphite oxide gel was dispersed in diluted hydrochloric acid by ultrasonication for 1 hour to obtain graphene oxide (GO) suspension, and the concentration of GO was adjusted to 2 mg mL^{-1}. Secondly, 0.05 mol L^{-1} aniline which was dispersed in 1.0 mol L^{-1} hydrochloric acid was slowly added into the GO suspension with ultra-sonication for 30 min, and ammonium persulfate was slowly added into the mixture. The molar ratio of aniline to ammonium persulfat and aniline to GO were 1:1 and 1:20, respectively. Finally, the mixture was stirred for 7 h in an ice bath; GO/PANI composite was obtained from the freeze-dried reaction production which was washed with alcohol, ether and ultrapure water in sequence. Pure PANI was also prepared by the same chemical process without GO.

The obtained GO/PANI composite was directly added into the GO suspensions to obtain the mixed suspensions, the mass ratio of GO suspensions to GO/PANI composite was set as 1:0.5-4.0, followed by ultra-sonication. After obtaining stable mixed suspensions, the suspensions were put into polytetrafluoroethyl-ene vessel (50 mL). The vessel was then sealed in a stainless steel autoclave and heated to 160 °C for 5 h. Followed by freeze-drying, 3DGP was obtained, and the digital picture of 3DGP is also presented in Fig.1. The obtained 3DGP samples were labelled as 3DGP-*n*, where *n* stands for the dosage of GO/PANI. Pure rGO was also prepared by the same chemical process only with GO suspensions.

3. Characterization

The images of scanning electron microscope (SEM) and transmission electron microscopy (TEM) were obtained on a ZEISS Ultra 55 microscopy and Zeiss Libra 200FE microscope, respectively. X-ray diffraction (XRD) patterns were measured on a PANalytical X'Pert PRO multifunctional powder diffract meter. Raman spectra were recorded on Renishaw InVia Raman Microprobe using a 514.5 nm Ar^+ laser. X-ray photoelectron spectra (XPS) were measured on a Kratos XSAM800 photoelectron spectrometer. Nitrogen adsorption-desorption isotherms were measured at 77 K using a Quantachrome Autosorb-1MP analyzer. Fourier transform infrared (FT-IR) spectra were recorded by a Nicolet5700 FT-IR spectrometer.

4. Electrochemical measurements

The obtained 3DGP was sliced to slices, the mass and dimensions of the slices are about 2 mg and 1 × 1 cm^2. The working electrodes were prepared by pressing the slices onto nickel foam (1×3 cm^2) under 8 MPa for 30 s. The electrodes were soaked for 2 h before the measurements.

The electrochemical measurements of the electrodes were determined in a three-electrode test cell, which contained a platinum foil electrode (1.5×1.5 cm^2) as counter electrode, 1 mol L^{-1} H_2SO_4 and 6 mol L^{-1} KOH aqueous solutions as electrolytes when reference electrodes are saturated calomel electrode (SCE) and Hg/HgO electrode, correspondingly. The cyclic voltammetry (CV), galvanostatic charge/discharge (GCD) electrochemical impedance spectroscopies (EIS) tests were carried out on a CHI660E electrochemical work station at room temperature. For the CV measurements of the rGO electrode, the sweep rate was 5 mV s^{-1} within a potential range of −1.0 to 0 V which was referenced to Hg/HgO. For the CV measurements of the 3DGP electrode, the sweep rate was 5 mV s^{-1} within a potential range of −0.2 to 0.8 V which was referenced to SCE. For the GCD measurements of rGO, the current density ranged from 0.5 to 20.0 A g^{-1}, the potential ranges were the same as CV measurements. For the GCD measurements of PANI and 3DGP, the current density ranged from 0.5 to 20.0 A g^{-1}, the potential ranged from -0.2 to 0.7 V. For the EIS measurements, the perturbation potential was 5 mV, the frequency ranged from 0.01 Hz to 100 kHz.

Results and discussion

1. Morphology and structure of rGO, PANI and 3DGP

The morphologies of rGO, PANI and 3DGP-2.0 were observed by SEM, TEM and HRTEM and their images are shown in Fig. 3. The SEM images of rGO in Fig. 3a and d reveal that the freeze-dried rGO has an interconnected 3D porous network. The pore sizes of the network ranging from sub-micrometers to several micrometers and the pore walls consisting of multi-layer graphene[43]. The TEM image of rGO in Fig. 3b reveals that the ultrathin sheets of rGO have wrinkled paper-like structures that graphene owns intrinsically[44]. The high resolution TEM image of rGO in Fig. 3c shows the enlarged wrinkles of graphene layers. The width of the wrinkle stripes indicates that rGO is composed of approximately 3-5 wrinkled monolayer graphene. In Fig. 3e and f, the prepared PANI shows uniform fibrous structures of hundreds of nanometers in length and about 30-50 nm in width. Fig. 3g shows the SEM image of 3DGP-2.0, the morphology of 3DGP-2.0 is similar to that of rGO. PANI fiber cannot be found in the SEM image because the fibers are in the graphene cladding. The TEM images of 3DGP in Fig. 3h and i show that the PANI nanofibers are dispersed evenly in the interlayer space of the graphene layers, PANI and rGO are signed with arrows. Similar morphology is also obtained from other 3DGP samples.

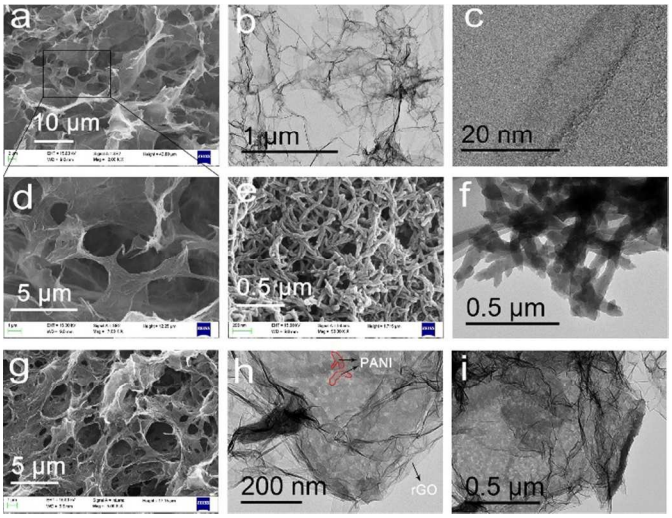

Fig. 3 SEM images of rGO (a and d), TEM (b) and HRTEM (c) images of rGO, SEM(e) and TEM (f) images of PANI, SEM (g) and TEM (h and i) images of 3DGP-2.0.

XRD pattern of 3DGP-2.0 in Fig. S1a exhibits one peak similar to that of rGO, but the peak of 3DGP-2.0 is much wider than that of rGO, indicating that the 3DGP composite exhibits worse crystallinity than that of pure rGO, so it can be implied that PANI is wrapped in the rGO interlayers which can decrease the order degree of rGO. The results of Ramman spectra in Fig. S1b suggest that the benzenoid unit concentration is increased in 3DGP-2.0, which gives evidence that a π-π interaction occurs between the quinoid ring of PANI and graphene which can influence the electronic transport properties of the 3DGP. The N1s peak in the XPS spectra of 3DGP-2.0 in Fig. S2 can also give evidence that PANI is presented in the composite and the same conclusin can also be abtained from the results of FT-IR in Fig.S3. The results of BET in Fig.S4 shows that the por size of 3DGP-2.0 composite mainly center around 3.0 nm. Because of PANI is wrapped in graphene layers, the BET surface of 3DGP-2.0, 177.5 m^2 g^{-1}, is lager than that of either pure rGO ,65.13 m^2 g^{-1}, or pure PANI,48.5 m^2 g^{-1}.

The XRD patterns, and FT-IR spectra of other 3DGP samples in Fig.S5 can also conclude that PANI is to certain degree presented in the graphene layers. The detail information is also supplied in the surpporting information.

2. Electrochemical performances

Fig. 4a shows the CV curves of rGO, PANI and 3DGP-2.0 electrodes at 5 mV s^{-1}. The CV curve of rGO electrode in Fig. 4a inset exhibits an approximately rectangular shape that is characteristic of the electrical double-layer capacitance[45]. In the curves of PANI and 3DGP-2.0, two couples of redox peaks (P_1, P_2, P_3, P_4) are observed, corresponding to redox transition of fleuco emeraldine (semiconductor)/polaronic emeraldine (conductor) and faradic transformation of emeraldine/pernigraniline[46, 47], respectively. 3DGP-2.0 electrode exhibits a combination of both EDLC and pseudocapacitor[28]. Compare with pure PANI, a deviation of the redox peaks has been found which is due to the interaction between rGO and PANI[25]. It is commonly believed that the electrochemical capacitance is proportional to the area of the CV curve. The CV curve area of the 3DGP-2.0 is larger than that of pure PANI, indicating that the addition of rGO improves the capacity of 3DGP-2.0 electrode. Fig. 4b shows CV curves of 3DGP-2.0 at different scan rates. It can be noted that the area of CV curves increase with the scan rate and the CV curves almost maintain the same shape, indicating 3DGP-2.0 electrode has good rate capability. The CV curves of all the prepared 3DGP samples with different dossage of GO/PANI are presented in Fig.S6 .Compared with other 3DGP samples, the CV curve of 3DGP-2.0 has the largest area at 5.0 mV s^{-1} indicates that 3DGP-2.0 has the highest specfic capacitance.

Fig. 5a shows the GCD curves at 1.0 A g^{-1}. The curves of rGO deviate from regular triangular-shape, corresponding to the typical characteristics of EDLC[45]. However, the curve of the pure PANI exhibits a voltage drop which originated from the faradaic reactions. The GCD curve of 3DGP clearly demonstrates that the charge and discharge time is longer than that of PANI and rGO electrodes, indicating that the effective energy storage is improved. The specific capacitance can be calculated from the GCD curves using equation: $C=I\Delta t/m\Delta V$, where I is the current of charge/discharge, Δt is the time of discharge, m is the mass of active materials in the working electrode, and ΔV is the potential window. Fig. 5b shows the specific capacities at different current densities. The specific capacitance for pure PANI, rGO and 3DGP-2.0 at 0.5 A g^{-1} is 311, 303 and 648 F g^{-1}, respectively. The specific capacitance of 3DGP is much higher than those of pure PANI and rGO. When the current density is greater than 10.0 A g^{-1}, the specific capacitance of pure PANI verges to zero. However, the specific capacitance of 3DGP-2.0 retains 356 F g^{-1} even at 20.0 A g^{-1}, which indicates good rate capability for 3DGP-2.0. Fig. 5c shows the long cycling performance at 1.0 A g^{-1} for rGO, PAIN and 3DGP electrodes. The specific capacitance of pure PANI, rGO and 3DGP decrease from 256, 280 and 610 to 115, 255 and 537 F g^{-1} after 1000 cycles respectively, which corresponds to 44%, 91% and 88% of their initial values. It is noted that the capacitance retention rate of 3DGP is higher than that of pure PANI which due to the contribution of rGO because it can improve the electrical conductivity of the electrode material. The GCD curves and specific capacities at different current densities of all the prepared 3DGP samples with different dossage of GO/PANI are presented in Fig.S7. It indicates that 3DGP-2.0 has the best capacity performance which agree with the CV results well.

Electrochemical impedance spectroscopy (EIS) is considered as an efficient technique to evaluate the properties of conductivity, structure and charge transport in the electrolyte interface. Fig. 5d

shows the Nyquist plots of PAIN and 3DGP-2.0 electrodes. The impedance behaviour might be dominated by three major processes occurring in the high, medium and low frequency regions, respectively[48]. The radius of semicircle in the high frequency region for pure PANI is larger than that for 3DGP, which indicates the polarization resistance of pure PANI is higher than that of 3DGP, owing to the highly electrical conductive 3D network of rGO inside the composites[49]. At medium frequency region, the larger Warburg region of PANI than that of 3DGP indicates greater variations in ion diffusion path lengths which increase the obstruction of ion movement. At low frequency, the imaginary part of the impedance curves for both electrodes approach a vertical line, indicating a typical capacitive-type behaviour.

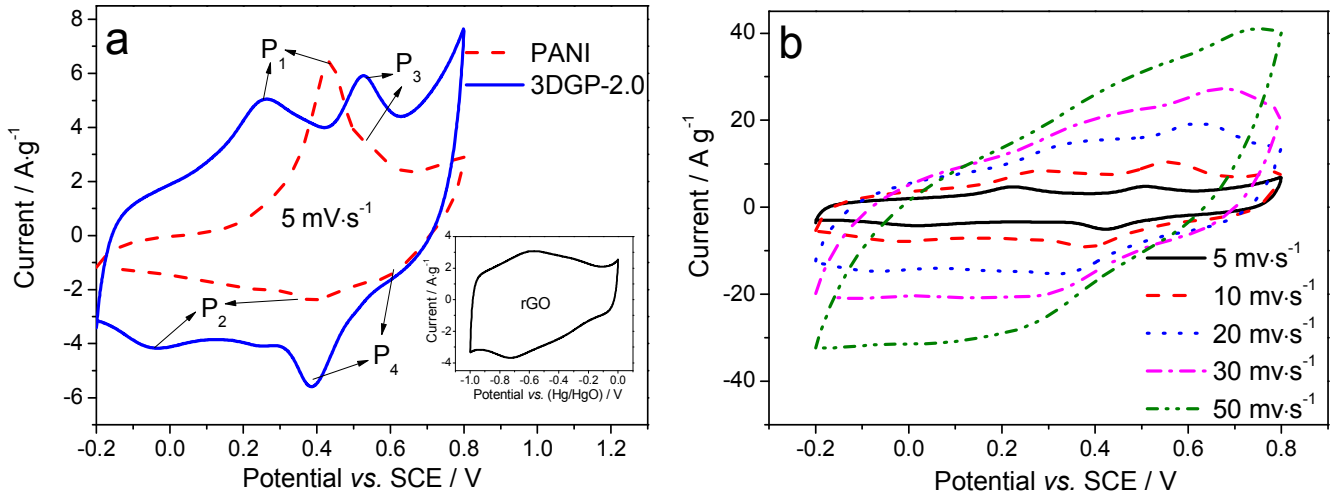

Fig.4 (a) Cyclic voltammetry (CV) curves of rGO, PANI and 3DGP-2.0 electrodes at 5 mV s^{-1}; (b) CV curves of 3DGP-2.0 electrode at different scan rate of 5 mV s^{-1}, 10 mV s^{-1}, 20 mV s^{-1}, 30 mV s^{-1} and 50 mV s^{-1}, respectively.

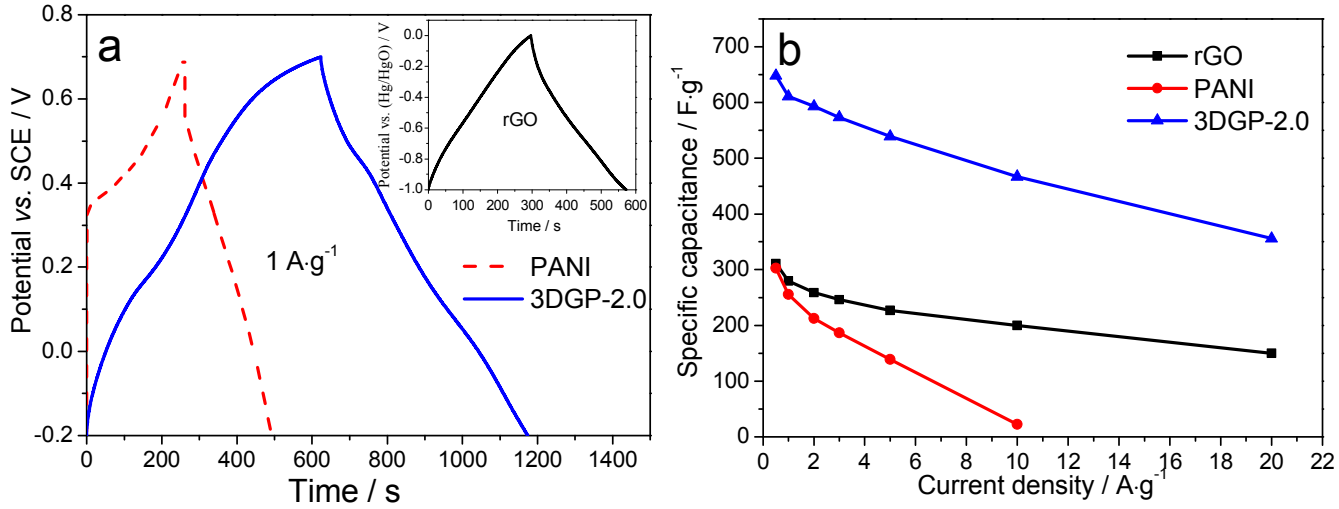

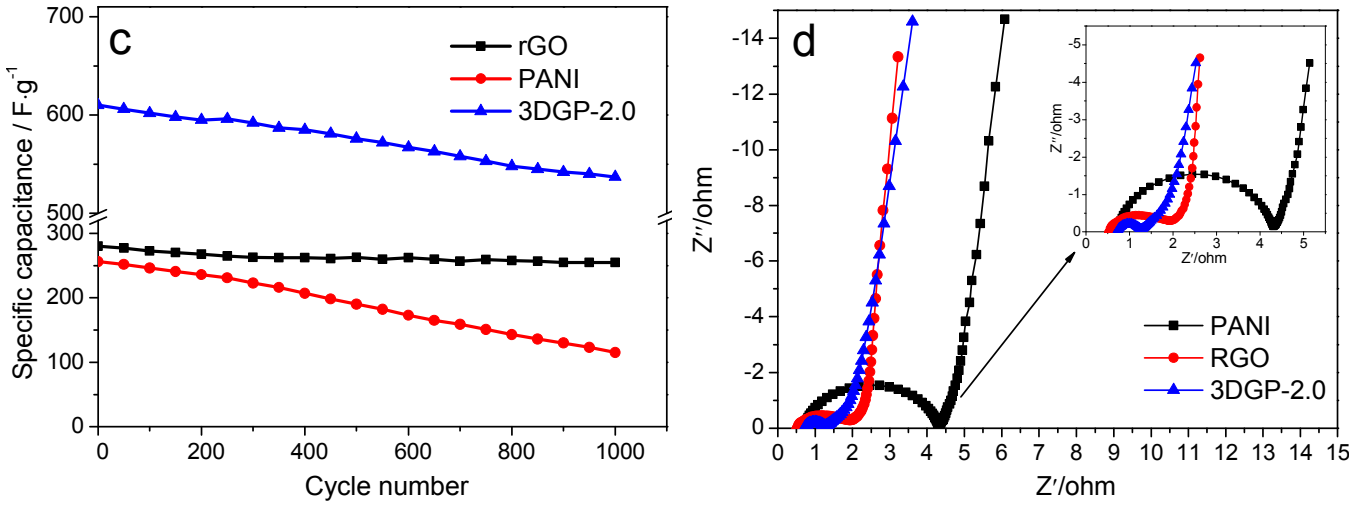

Fig. 5 (a) Galvanostatic charge/discharge curves at 1.0 A g^{-1}, (b) specific capacities at different current densities, (c) cycling performance at 1.0 A g^{-1} for rGO, PAIN and 3DGP electrodes and (d) Nyquist plots of PAIN and 3DGP-2.0 electrodes.

Fig. 6 compared the specific energy density (E) and power density (P) of PANI, rGO and 3DGP-2.0 composite. E and P are caculated according to Equations[50]: $E = (C_m V^2)/4$ and $P = E/t$, where C_m is the specific capacitance of the composite electrode, t is the discharge time and V is the potential range. As shown in Fig. 6, the specific energy densities of the three electrodes reduce slowly with increasing of power densities. The energy density of 3DGP-2.0 composite can reach 73 Wh kg^{-1} at a power density of 223.7 W kg^{-1}, and still remains 40.1 Wh kg^{-1} at a power density of 9022.5 W kg^{-1}. Its energy density is higher than that of PANI, rGO. Thus, the 3DGP is proved to be an effective strategy in preparing the PANI/graphene composite with good supercapacitive performance.

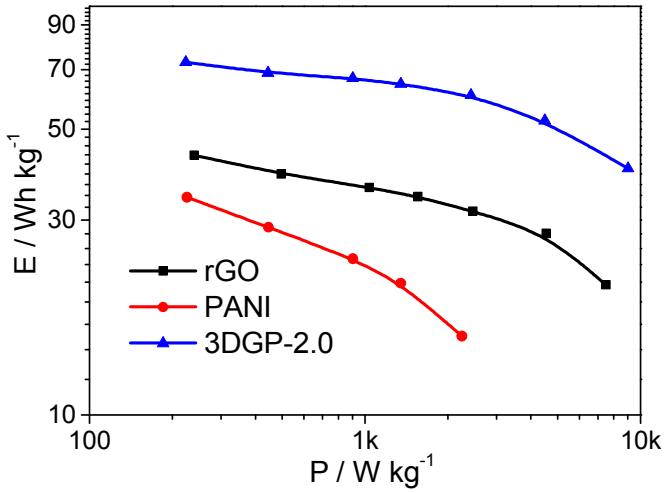

Fig. 6 Ragone plots of specific power vs. specific energy for rGO, PANI and 3DGP-2.0 electrodes.

Conclusions

A novel 3DGP composite was achieved by hydrothermal method from in-situ polymerization PANI/GO composite and GO suspension. This 3DGP composite possesses a 3D porous network structure and a large specific capacity of 648 F g^{-1} at a current density of 0.5 A g^{-1}. Particularly, the capability can reach 356 F g^{-1} even at 20.0 A g^{-1}, 537 F g^{-1} at 1.0 A g^{-1} can also be achieved after 1000 cycles. Therefore, the 3DGP composite is quite a suitable and promising electrode material for supercapacitors.

Acknowledgements

This work was supported by National Natural Science Foundation of China (Grant No. 41272051), Postgraduate Innovation Fund Project by Southwest University of Science and Technology (Grant No.14ycx003), Doctor Foundation of Southwest University of Science and Technology (Grant No. 11ZX7135), and the Miaozi Subtopic Project for the Construction of Mianyang Sci-tech City University Students' Innovative Undertaking Club Demonstration Site (Grant No. 2014RZ0038-15).

Notes and references

[a] Institute of Mineral Materials & Application, Southwest University of Science and Technology, Mianyang 621010, P.R. China.
[b] School of Material Science and Engineering, Southwest University of Science and Technology, Mianyang 621010, P.R. China.
[c] Wenshang NO.1 Experimental Middle School, Jining 272500, P.R. China.
† These authors contributed equally to this work.
* Corresponding author, E-mail: tjpeng@swust.edu.cn.
Electronic Supplementary Information (ESI) available, See DOI: 10.1039/b000000x/

1. R. Kötz and M. Carlen, *Electrochimica Acta*, 2000, **45**, 2483-2498.
2. P. Simon and Y. Gogotsi, *Nat Mater*, 2008, **7**, 845-854.
3. Y. Soneda, M. Kodama and T. Morishita, Google Patents, 2013.
4. H. X. Ji, X. Zhao, Z. H. Qiao, J. Jung, Y. W. Zhu, Y. L. Lu, L. L. Zhang, A. H. MacDonald and R. S. Ruoff, *Nature Communications*, 2014, **5**.
5. Y. H. Lee, K. H. Chang and C. C. Hu, *Journal Of Power Sources*, 2013, **227**, 300-308.

6. D. Aradilla, G. Bidan, P. Gentile, P. Weathers, F. Thissandier, V. Ruiz, P. Gomez-Romero, T. J. S. Schubert, H. Sahin and S. Sadki, *Rsc Advances*, 2014, **4**, 26462-26467.
7. M. Wang, W. Wang, W. Wang and X. Guo, *RSC Advances*, 2014, **4**, 39625-39633.
8. M. Lu, F. Beguin and E. Frackowiak, *Supercapacitors: Materials, Systems and Applications*, John Wiley & Sons, 2013.
9. A. Djire, O. T. Ajenifujah, A. Sleightholme, P. Rasmussen and L. T. Thompson, in *Meeting Abstracts*, The Electrochemical Society, 2014, pp. 196-196.
10. G. Xiong, C. Meng, R. G. Reifenberger, P. P. Irazoqui and T. S. Fisher, *Electroanal*, 2014, **26**, 30-51.
11. C. Peng, S. Zhang, D. Jewell and G. Z. Chen, *Progress in Natural Science*, 2008, **18**, 777-788.
12. D. W. Wang, F. Li, M. Liu, G. Q. Lu and H. M. Cheng, *Angew Chem Int Edit*, 2008, **47**, 373-376.
13. L. L. Zhang and X. Zhao, *Chemical Society Reviews*, 2009, **38**, 2520-2531.
14. T. M. Higgins, D. McAteer, J. C. M. Coelho, B. M. Sanchez, Z. Gholamvand, G. Moriarty, N. McEvoy, N. C. Berner, G. S. Duesberg and V. Nicolosi, *ACS nano*, 2014.
15. X.-h. Xia, J.-p. Tu, Y.-q. Zhang, Y.-j. Mai, X.-l. Wang, C.-d. Gu and X.-b. Zhao, *Rsc Advances*, 2012, **2**, 1835-1841.
16. R. Ranjusha, S. Ramakrishna, A. S. Nair, P. Anjali, S. Vineeth, T. S. Sonia, N. Sivakumar, K. R. V. Subramanian, S. V. Nair and A. Balakrishnan, *Rsc Advances*, 2013, **3**, 17492-17499.
17. G. Xiong, K. P. S. S. Hembram, R. G. Reifenberger and T. S. Fisher, *Journal of Power Sources*, 2013, **227**, 254-259.
18. C. He, Y. Xiao, H. Dong, Y. Liu, M. Zheng, K. Xiao, X. Liu, H. Zhang and B. Lei, *Electrochimica Acta*, 2014, **142**, 157-166.
19. Z. Gao, F. Wang, J. Chang, D. Wu, X. Wang, X. Wang, F. Xu, S. Gao and K. Jiang, *Electrochimica Acta*, 2014, **133**, 325-334.
20. S. Yang, X. Song, P. Zhang and L. Gao, *ACS applied materials & interfaces*, 2013, **5**, 3317-3322.
21. P. Si, S. J. Ding, X. W. Lou and D. H. Kim, *Rsc Advances*, 2011, **1**, 1271-1278.
22. G. Xiong, C. Meng, R. G. Reifenberger, P. P. Irazoqui and T. S. Fisher, *Adv Energy Mater*, 2014, **4**, n/a-n/a.
23. H. Mi, X. Zhang, S. An, X. Ye and S. Yang, *Electrochemistry Communications*, 2007, **9**, 2859-2862.
24. C. Meng, C. Liu and S. Fan, *Electrochemistry Communications*, 2009, **11**, 186-189.
25. Y. S. Luo, D. Z. Kong, Y. L. Jia, J. S. Luo, Y. Lu, D. Y. Zhang, K. W. Qiu, C. M. Li and T. Yu, *Rsc Advances*, 2013, **3**, 5851-5859.
26. X. M. Feng, R. M. Li, Y. W. Ma, R. F. Chen, N. E. Shi, Q. L. Fan and W. Huang, *Advanced Functional Materials*, 2011, **21**, 2989-2996.
27. H.-P. Cong, X.-C. Ren, P. Wang and S.-H. Yu, *Energy & Environmental Science*, 2013, **6**, 1185-1191.
28. Q. Q. Zhou, Y. R. Li, L. Huang, C. Li and G. Q. Shi, *Journal Of Materials Chemistry A*, 2014, **2**, 17489-17494.
29. J. J. Cong, Y. Z. Chen, J. Luo and X. Y. Liu, *J Solid State Chem*, 2014, **218**, 171-177.
30. P.-J. Hung, K.-H. Chang, Y.-F. Lee, C.-C. Hu and K.-M. Lin, *Electrochimica Acta*, 2010, **55**, 6015-6021.
31. Q. Wu, Y. X. Xu, Z. Y. Yao, A. R. Liu and G. Q. Shi, *Acs Nano*, 2010, **4**, 1963-1970.
32. S. Liu, X. H. Liu, Z. P. Li, S. R. Yang and J. Q. Wang, *New J Chem*, 2011, **35**, 369-374.
33. S. P. Zhou, H. M. Zhang, Q. Zhao, X. H. Wang, J. Li and F. S. Wang, *Carbon*, 2013, **52**, 440-450.
34. J. Li, H. Q. Xie, Y. Li, J. Liu and Z. X. Li, *Journal Of Power Sources*, 2011, **196**, 10775-10781.
35. D. W. Wang, F. Li, J. P. Zhao, W. C. Ren, Z. G. Chen, J. Tan, Z. S. Wu, I. Gentle, G. Q. Lu and H. M. Cheng, *Acs Nano*, 2009, **3**, 1745-1752.
36. X. M. Feng, R. M. Li, Y. W. Ma, R. F. Chen, N. E. Shi, Q. L. Fan and W. Huang, *Advanced Functional Materials*, 2011, **21**, 2989-2996.
37. L. W. Hu, J. G. Tu, S. Q. Jiao, J. G. Hou, H. M. Zhu and D. J. Fray, *Physical Chemistry Chemical Physics*, 2012, **14**, 15652-15656.
38. G. Xiong, K. P. S. S. Hembram, D. N. Zakharov, R. G. Reifenberger and T. S. Fisher, *Diamond and Related Materials*, 2012, **27–28**, 1-9.
39. M. A. Worsley, S. O. Kucheyev, H. E. Mason, M. D. Merrill, B. P. Mayer, J. Lewicki, C. A. Valdez, M. E. Suss, M. Stadermann and P. J. Pauzauskie, *Chem. Commun.*, 2012, **48**, 8428-8430.
40. Y. Xu, Z. Lin, X. Huang, Y. Wang, Y. Huang and X. Duan, *Advanced Materials*, 2013, **25**, 5779-5784.
41. Z. Niu, L. Liu, L. Zhang, Q. Shao, W. Zhou, X. Chen and S. Xie, *Advanced Materials*, 2014.
42. H. Xian, T. Peng, H. Sun and J. Wang, *Nano-Micro Letters*, 2014, **7**.
43. Y. X. Xu and G. Q. Shi, *Journal Of Materials Chemistry*, 2011, **21**, 3311-3323.
44. F. Schedin, A. Geim, S. Morozov, E. Hill, P. Blake, M. Katsnelson and K. Novoselov, *Nature materials*, 2007, **6**, 652-655.
45. T. Kim and R. S. Ruoff, in *Meeting Abstracts*, The Electrochemical Society, 2014, pp. 1147-1147.
46. K. Zhang, L. L. Zhang, X. Zhao and J. Wu, *Chemistry of Materials*, 2010, **22**, 1392-1401.
47. A. Eftekhari and B. Yazdani, *Journal of Polymer Science Part A: Polymer Chemistry*, 2010, **48**, 2204-2213.
48. M. Adachi, M. Sakamoto, J. Jiu, Y. Ogata and S. Isoda, *The Journal of Physical Chemistry B*, 2006, **110**, 13872-13880.
49. X. H. Cao, Y. M. Shi, W. H. Shi, G. Lu, X. Huang, Q. Y. Yan, Q. C. Zhang and H. Zhang, *Small*, 2011, **7**, 3163-3168.
50. H.-Q. Li, J.-Y. Luo, X.-F. Zhou, C.-Z. Yu and Y.-Y. Xia, *Journal of the Electrochemical Society*, 2007, **154**, A731-A736.

